

***Ab initio* calculation of the reflectivity of molecular fluids under shock compression**Martin French ¹, Mandy Bethkenhagen ^{2,3}, Alessandra Ravasio,⁴ and Jean-Alexis Hernandez ⁵¹*Universität Rostock, Institut für Physik, Albert-Einstein-Str. 23-24, D-18059 Rostock, Germany*²*École Normale Supérieure, Université Lyon 1, Laboratoire de Géologie de Lyon, CNRS UMR 5276, 69364 Lyon Cedex 07, France*³*Institute of Science and Technology Austria, Am Campus 1, 3400 Klosterneuburg, Austria*⁴*LULI, CNRS, CEA, Sorbonne Université, Ecole Polytechnique - Institut Polytechnique de Paris, 91128 Palaiseau, France*⁵*European Synchrotron Radiation Facility, 71 avenue des Martyrs, 38000 Grenoble, France*

(Received 7 December 2022; revised 9 March 2023; accepted 9 March 2023; published 13 April 2023)

We calculate reflectivities of dynamically compressed water, water-ethanol mixtures, and ammonia at infrared and optical wavelengths with density functional theory and molecular dynamics simulations. The influence of the exchange-correlation functional on the results is examined in detail. Our findings indicate that the consistent use of the HSE hybrid functional reproduces experimental results much better than the commonly used PBE functional. The HSE functional offers not only a more accurate description of the electronic band gap but also shifts the onset of molecular dissociation in the molecular dynamics simulations to significantly higher pressures. We also highlight the importance of using accurate reference standards in reflectivity experiments and reanalyze infrared and optical reflectivity data from recent experiments. Thus, our combined theoretical and experimental work explains and resolves lingering discrepancies between calculations and measurements for the investigated molecular substances under shock compression.

DOI: [10.1103/PhysRevB.107.134109](https://doi.org/10.1103/PhysRevB.107.134109)**I. INTRODUCTION**

Apart from smaller amounts of helium and rock-forming materials, the solar giant planets are primarily composed of molecular substances, e.g., hydrogen [1,2] in case of Jupiter and Saturn or water, ammonia, and methane in case of Uranus [3] and Neptune [4]. Their interiors host extreme pressures p in the megabar range and temperatures T of several thousand Kelvin, which causes substantial dissociation and ionization of molecular substances. Such processes disrupt the electronic structure of molecules and release free charge carriers, which leads to electrical conductivities σ high enough to support the generation of strong magnetic fields on a planetary scale [5–8].

Dynamic compression experiments [9,10] are powerful tools for generating high pressures and high temperatures and allow us to probe the properties of matter at extreme conditions. Especially in the second half of the 20th century, the dc conductivity of dynamically compressed materials was measured in a few experiments propelled with mechanical shock drivers [11–18]. However, the relatively long timescales involved in such measurements prevent similar measurements in novel laser-driven and Z-pinch experiments [19]. Instead, new designs were developed to measure shock-front reflectivities at infrared and optical frequencies ω [20–32], which are directly related to the electrical conductivity. Inferring the corresponding dc conductivity values from the reflectivity is very challenging, though, because the required frequency dispersion function toward $\omega \rightarrow 0$ is unknown.

In practice, reflectivity measurements are done in initially transparent samples, which become reflective under compression. The shock front reflectivity is measured by reflection of a probe laser both inside the sample and inside a reference

material with known reflectivity under shock, such as quartz, which is used to quantify the measured sample reflectivity on an absolute scale. By performing reflectivity measurements simultaneously at different wavelengths (generally two for practical reasons), the frequency dependence of the reflectivity can be probed. The electronic dc conductivity is typically estimated by assuming a Drude model, see e.g., Ref. [33], or by combining both experimental reflectivities and qualitative inputs from *ab initio* simulations on the frequency dependence of the complex conductivity and its evolution as function of pressure and temperature [29]. Note that a Drude-like frequency behavior is reasonable only for conduction electrons in relatively cold materials that are characterized by a single relaxation time that represents their scattering properties at the Fermi level, but not in thermally excited materials or plasmas [34], or when bound states play a role [35].

Theoretical approaches to calculate the electrical conductivity and optical properties have to describe the electronic structure of matter with sufficient accuracy and incorporate effects of pressure and temperature. A combination of density functional theory (DFT) for thermal electrons [36–38] and classical molecular dynamics (MD) for the ions has proven to be an appropriate method to accomplish this task [30,39–43]. Yet, these calculations are susceptible to approximations, especially regarding the exchange-correlation (XC) functional in DFT.

The XC functional describes many-particle quantum and correlation effects in the electronic structure. Different levels of approximations for XC were developed [44,45], and they offer different qualities in predicting particular material properties. While semilocal XC functionals like the PBE functional usually yield good lattice constants and molecular geometries [46,47] with moderate computational effort, they

underestimate semiconductor band gaps [48,49], which makes them a poor choice for calculating conductivities and optical properties of nonmetals. Hybrid functionals like the HSE functional [50,51] can remedy this drawback to a large extent [48,49] and also increase the accuracy of calculated lattice constants even further [47,48]. A disadvantage of hybrid functionals is that they are much more computationally expensive (about 25 times slower than PBE in our case). This has yet prevented extensive use of these functionals in applications where long DFT-MD simulations need to be carried out.

Here we explore the influence of the XC functional on DFT-MD calculations for water, water-ethanol mixtures, and ammonia. We especially elaborate its effect on ionic configurations generated in the DFT-MD separately from its influence on the subsequent static DFT calculations for the optical properties. The consequent use of the HSE hybrid functional instead of the PBE functional [52] shifts dissociation and ionization transitions to higher $p - T$ conditions in all calculations. In comparison with recent and partially reanalyzed experiments (see Sec. III for details), we conclude that the HSE functional offers a strongly improved description of the optical properties of molecular mixtures.

Since both PBE and HSE functional are approximations for the ground-state XC energy, our paper does not discuss the influence of thermal effects in the XC functional for the electronic free energy [53–55]. Such effects become relevant usually as the thermal energy approaches the Fermi energy and vanish again at higher temperatures as the classical ideal gas limit is reached. Thermal XC effects can influence thermodynamic and transport properties of warm dense matter to some extent, but their magnitude is hardly resolvable with present experimental methods [56–60]. To our knowledge, no thermal XC functional for the free energy has been developed that can reach the performance of hybrid functionals like HSE in ground-state DFT calculations, so far.

II. THEORETICAL METHOD

The following two subsections describe the theoretical method in greater detail and are focused on the DFT-MD simulations, Sec. II A, and on the calculation of the optical properties, Sec. II B.

A. DFT-MD simulations

Our DFT-MD calculations are performed with the Vienna *Ab initio* Simulation Package (VASP) 5.4.4 [61–64], in which the electronic wave functions are expanded in plane waves and the electron-ion interaction is treated with projector-augmented wave (PAW) pseudopotentials [65,66]. In the DFT-MD simulations that are used to generate equation of state (EOS) data and ionic configurations for subsequent calculations of optical properties, we use the following PAW pseudopotentials: the PAW_PBE H_h for hydrogen, the PAW_PBE C_h for carbon, the PAW_PBE N_h for nitrogen, and the PAW_PBE O_h for oxygen. The latter three pseudopotentials treat the $1s$ electrons as frozen and consider only the $2s$ and $2p$ electrons self-consistently in the DFT. The plane-wave cutoff is set to 1000 eV, which yielded very well-converged EOS results in previous work on mixtures

of water, ammonia, and methane [67]. The electronic wave functions are evaluated at the Baldereschi mean-value point [68]. Time steps for the ionic movements are chosen between 0.25 and 0.4 fs and the ion temperature is regulated with a Nosé-Hoover thermostat [69,70]. Simulation times amount to 5000 to few 100 000 time steps after equilibration, depending on complexity of the fluid and on temperature. The specific XC functional and particle numbers used will be reported in the sections for the individual substances. All simulation parameters were tested to ensure well converged DFT-MD results for both the PBE [52] and the HSE functional [50,51] with a Hartree-Fock screening parameter of $0.2/\text{Å}$.

Because the ions are approximated as classical particles that form molecules at low T , the caloric EOS (internal energy) u can become substantially inaccurate. Especially nuclear quantum effects in the intramolecular vibrational motion lower the heat capacity compared to that of a classical ion system simulated with DFT-MD. This drawback can be approximately compensated for by reincluding nuclear quantum effects via a postprocessing of the caloric EOS [71–73]. The procedure requires the calculation of the power spectrum of the nuclear motion from the ionic velocity autocorrelation functions $\langle \mathbf{v}_a(t) \cdot \mathbf{v}_a(0) \rangle$ via [71]

$$S(\omega, \varrho, T) = \sum_a \frac{4m_a N_a}{3Nk_B T} \int_0^\infty dt \cos(\omega t) \langle \mathbf{v}_a(t) \cdot \mathbf{v}_a(0) \rangle, \quad (1)$$

where N_a and m_a , respectively, are particle number and mass of nuclear species a , $N = \sum_a N_a$ is the total number of nuclei, ϱ is the mass density, ω the frequency, and k_B is the Boltzmann constant. In a molecular system, Eq. (1) reproduces the vibrational density of states as characteristic peaks, see Fig. 10 in Ref. [72] for an example.

The following expression [71–73]

$$u_{vc}(\varrho, T) = \frac{3N}{2\pi m} \int_0^\infty d\omega S(\omega, \varrho, T) \times \left[\hbar\omega \left(\frac{1}{2} + \frac{1}{\exp(\hbar\omega/k_B T) - 1} \right) - k_B T \right], \quad (2)$$

where $m = \sum_a m_a N_a$ is the total mass and \hbar is the Planck constant, represents a possibility to correct the internal energy for vibrational quantum effects in harmonic approximation. It adds the energy of a quantum harmonic oscillator and subtracts that of a classical harmonic oscillator $k_B T$ in each frequency interval. Such a postprocessing procedure has proven to yield significantly improved Hugoniot temperatures for ammonia [72] and water [74]; in the latter case it was applied in a simplified version. The thermodynamic inconsistency introduced by this procedure in the EOS for the pressure is very small and influences the resulting Hugoniot curves only weakly [72,74].

After adding u_{vc} to the internal energy calculated in the DFT-MD simulations, the Hugoniot curve is determined from the generated EOS data by solving the equation [9,75]

$$2(u - u_0) = (p + p_0)(\varrho_0^{-1} - \varrho^{-1}), \quad (3)$$

where the quantities indexed with 0 constitute initial conditions.

B. Calculation of optical properties with DFT

The focus of this paper is put on optical properties. These are derived with static DFT calculations using typically 25–60 ionic configurations from equilibrated DFT-MD simulations. First, we calculate the real part of the electronic conductivity with the frequency-dependent Kubo-Greenwood formula [76,77]

$$\sigma_1(\omega) = \frac{2\pi e^2}{3\omega V} \sum_{\mathbf{k}\nu\mu} |\langle \mathbf{k}\nu | \hat{\mathbf{v}} | \mathbf{k}\mu \rangle|^2 (f_{\mathbf{k}\mu} - f_{\mathbf{k}\nu}) \times \delta(E_{\mathbf{k}\nu} - E_{\mathbf{k}\mu} - \hbar\omega), \quad (4)$$

where e is the elementary charge, V is the volume of the simulation box, $E_{\mathbf{k}\mu}$ and $f_{\mathbf{k}\mu}$ are the eigenvalue and Fermi occupation number of the Bloch state $|\mathbf{k}\mu\rangle$, respectively. The matrix elements with the velocity operator $\langle \mathbf{k}\nu | \hat{\mathbf{v}} | \mathbf{k}\mu \rangle$ are calculated from the dipole matrix elements $\langle \mathbf{k}\nu | \hat{\mathbf{r}} | \mathbf{k}\mu \rangle$ via $\langle \mathbf{k}\nu | \hat{\mathbf{v}} | \mathbf{k}\mu \rangle = i(E_{\mathbf{k}\nu} - E_{\mathbf{k}\mu}) \langle \mathbf{k}\nu | \hat{\mathbf{r}} | \mathbf{k}\mu \rangle / \hbar$ [78]. The dipole matrix elements are computed by the optical routines of VASP and contain all nonlocal contributions from the PAW pseudopotentials and from the Hartree-Fock exchange [79]. The delta function is represented as a Gaussian function [80] with a finite width appropriate to generate sufficiently smooth functions.

Similarly, we calculate the imaginary part of the conductivity via

$$\sigma_2(\omega) = -\frac{2\pi \hbar e^2}{3V} \sum_{\mathbf{k}\nu\mu} |\langle \mathbf{k}\nu | \hat{\mathbf{v}} | \mathbf{k}\mu \rangle|^2 \frac{f_{\mathbf{k}\mu} - f_{\mathbf{k}\nu}}{E_{\mathbf{k}\mu} - E_{\mathbf{k}\nu}} \times \mathcal{P} \left(\frac{1}{E_{\mathbf{k}\nu} - E_{\mathbf{k}\mu} - \hbar\omega} \right). \quad (5)$$

This expression follows directly from the time integral that produces the δ function in the derivation of the real part (4) [81–84],

$$\begin{aligned} & \lim_{\varepsilon \rightarrow 0} \int_{-\infty}^0 dt \exp[(\varepsilon + i\omega + i\Delta E/\hbar)t] \\ &= \lim_{\varepsilon \rightarrow 0} \left[\frac{\varepsilon}{(\frac{\Delta E}{\hbar} + \omega)^2 + \varepsilon^2} - i \frac{\frac{\Delta E}{\hbar} + \omega}{(\frac{\Delta E}{\hbar} + \omega)^2 + \varepsilon^2} \right] \\ &= \hbar\pi \delta(\Delta E + \hbar\omega) - i\hbar \mathcal{P} \left(\frac{1}{\Delta E + \hbar\omega} \right), \end{aligned} \quad (6)$$

where $\Delta E = E_{\mathbf{k}\mu} - E_{\mathbf{k}\nu}$ and the broadening function from Eq. (6) is used when evaluating the principal value in Eq. (5). We have checked that the direct calculation of $\sigma_2(\omega)$ yields virtually the same results as a Kramers-Kronig transformation applied to $\sigma_1(\omega)$.

The conductivity $\sigma(\omega) = \sigma_1(\omega) + i\sigma_2(\omega)$ is directly related to the dielectric function $\epsilon(\omega) = \epsilon_1(\omega) + i\epsilon_2(\omega)$ through the equations $\epsilon_1(\omega) = 1 - \sigma_2(\omega)/\epsilon_0\omega$ and $\epsilon_2(\omega) = \sigma_1(\omega)/\epsilon_0\omega$, where ϵ_0 is the vacuum permittivity [85].

The complex index of refraction $n(\omega) + ik(\omega) = [\epsilon_1(\omega) + i\epsilon_2(\omega)]^{1/2}$ is then gained by

$$n(\omega) = \sqrt{\frac{1}{2} [|\epsilon(\omega)| + \epsilon_1(\omega)]}, \quad (7)$$

$$k(\omega) = \sqrt{\frac{1}{2} [|\epsilon(\omega)| - \epsilon_1(\omega)]}. \quad (8)$$

Finally, we obtain the reflectivity of a laser at a planar shock front from the Fresnel formula

$$R(\omega) = \frac{[n(\omega) - n_0(\omega)]^2 + [k(\omega) - k_0(\omega)]^2}{[n(\omega) + n_0(\omega)]^2 + [k(\omega) + k_0(\omega)]^2}, \quad (9)$$

where the quantities indexed with 0 correspond to the initial conditions of the Hugoniot experiment. Because all of our materials are optically transparent in the initial state, their absorption coefficients k_0 are essentially zero at the wavelengths of interest (1064 and 532 nm).

In the numerical DFT calculations, we use the following PAW pseudopotentials: the PAW_PBE H_h_GW for hydrogen, the PAW_PBE C_h_GW for carbon, the PAW_PBE N_h_GW for nitrogen, and the PAW_PBE O_h_GW for oxygen with a cutoff energy of 800 eV. These pseudopotentials are recommended for the calculations of optical properties but we have found only marginal differences in test calculations with the analogous set of pseudopotentials used in the DFT-MD calculations in Sec. II A. The \mathbf{k} -point sum in Eqs. (4) and (5) was restricted to the Baldereschi point [68]. The static DFT calculations were run with at least 80 eV of bands with a thermal occupation number less than 0.00001. Proper choice of all numerical parameters, including the number of bands, was checked with systematic convergence tests.

III. REANALYSIS OF REFLECTIVITY MEASUREMENTS IN SHOCKED WATER, WATER-ETHANOL MIXTURES, AND AMMONIA

Within two larger collaborations, we had previously performed reflectivity measurements in laser-shocked water, water-ethanol mixtures (WEM) [29], and ammonia [30] at the GEKKO XII (ILE, Osaka, Japan) and LULI2000 (Ecole Polytechnique, Palaiseau, France) laser facilities. Single shot reflectivities had been measured using both velocity reflectometer for any reflector (VISAR) channels at 532 nm (GEKKO XII and LULI2000) and 1064 nm (LULI2000) and a reflectometer at 532 nm (time-dependent measurement without interference fringes; LULI2000) following the same procedure as described in the Supplemental Material of our previous studies [30,32]. For a given shot, the measured normalized reflectivity had been scaled to the expected reflectivity of shocked quartz. At 532 nm, we had used the quartz reference models of Millot *et al.* [86] for water and WEM, and of Brygoo *et al.* [87] for ammonia. Both models are very close to each other, see Fig. 1, and are based on experimental data taken at the Omega laser facility (LLE, Rochester) [86,88]. At 1064 nm, the reflectivity of shocked quartz is poorly constrained as only one measurement from Huser *et al.* [89] has been reported for shock velocities U_s^{qz} ranging between 10.5 and 16.5 km/s.

In previous analyses of reflectivities of shocked water [29], WEM [29], and ammonia [30], we had used Huser *et al.*'s [89] experimental data as reference for the shocked quartz reflectivity at 1064 nm. However, Huser *et al.*'s [89] reflectivities at 532 nm are around 30% higher than previous experiments [88] and Brygoo *et al.*'s model [87] in the range

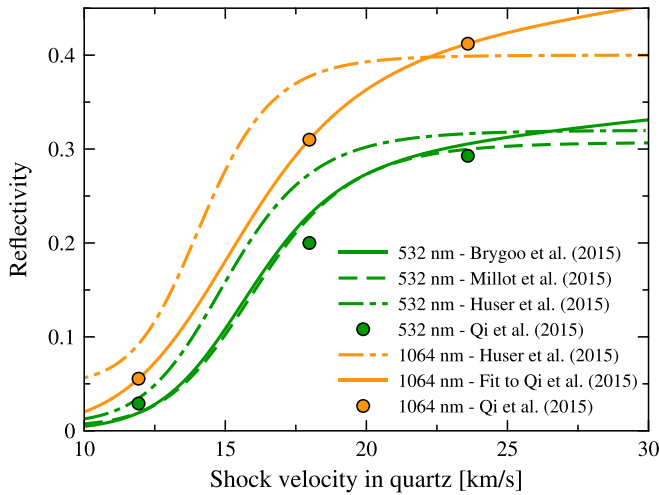


FIG. 1. Comparison of reflectivity models for shocked quartz at 1064 nm and 532 nm reported in the literature [86,87,89,90].

$U_s^{qz} \sim 10 - 20$ km/s. This discrepancy is similar to the one between Huser *et al.*'s data [89] and DFT-based calculations of Qi *et al.* [90] at 1064 nm. As Qi *et al.*'s data [90] closely match Brygoo *et al.*'s experimental model [87] at 532 nm, we suggest the reflectivity measured by Huser *et al.* [89] are overestimated at both wavelengths. For this reason, we adopt Qi *et al.*'s model [90] at 1064 nm in the present data reanalysis.

To recapitulate our previous experiments [29,30], we had used the experiment-based model of Ref. [89] as a reference scale to determine the reflectivities of water, WEM, and ammonia in our previous experiments at 1064 nm. Curiously, the reflectivities for water and ammonia along their principal Hugoniot curves were in excellent agreement with computed reflectivities (PBE-MD + HSE optics) at 1064 nm but not at 532 nm, where the computed reflectivities were somewhat lower than the measured ones, especially close to the onset of rising reflectivity [29,30]. At that time, the origin of these

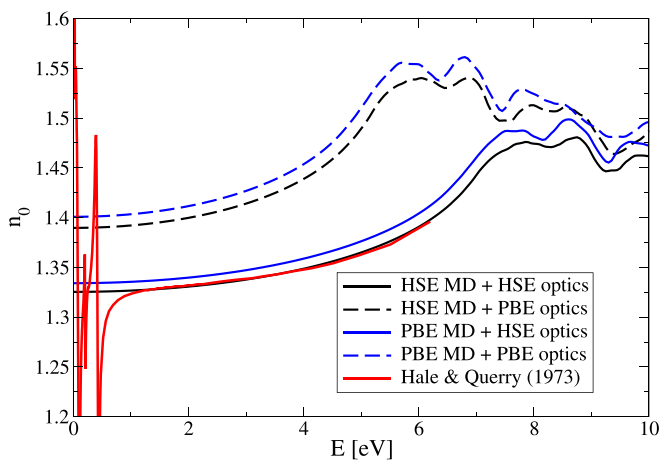


FIG. 2. Refractive index of water at the initial condition of 0.998 g/cm^3 and 298 K from DFT for the four possible combinations of PBE and HSE in DFT-MD and DFT optics calculations in comparison with the measurement by Hale and Query [91].

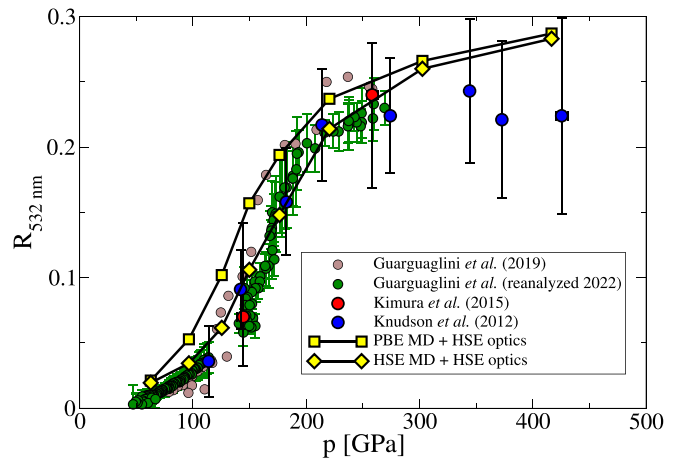


FIG. 3. 532-nm reflectivity along the principal Hugoniot curve of water compared with the experiments of Knudson *et al.* [25], Kimura *et al.* [26], and Guarguaglini *et al.* [29]. The data from Guarguaglini *et al.* [29] were reanalyzed in this paper according to Sec. III.

wavelength-dependent discrepancies between the computed and measured reflectivities could not be explained.

In the present study, we show reanalyzed reflectivities of water, WEM, and ammonia along their Hugoniot curves by considering Qi *et al.*'s model for reflectivity of shocked quartz at 1064 nm [90] instead of Huser *et al.*'s [89] results. Interestingly, rescaling the experimental reflectivities at 1064 nm based on Qi *et al.*'s model for quartz [90] lowers the reflectivity of shocked ammonia and results in a similar discrepancy with PBE-MD + HSE-optics calculations as found at 532 nm, which is at least more consistent, see also Fig. 12.

In addition, we also reanalyze water and WEM results using the same data extraction and analysis procedure as used for ammonia and described in Refs. [30,32]. Respective results are shown in Figs. 3, 4, 7, and 8 and are discussed in the following sections. This updated procedure differs to the one used in Ref. [29] by the time sampling of the data (resampling

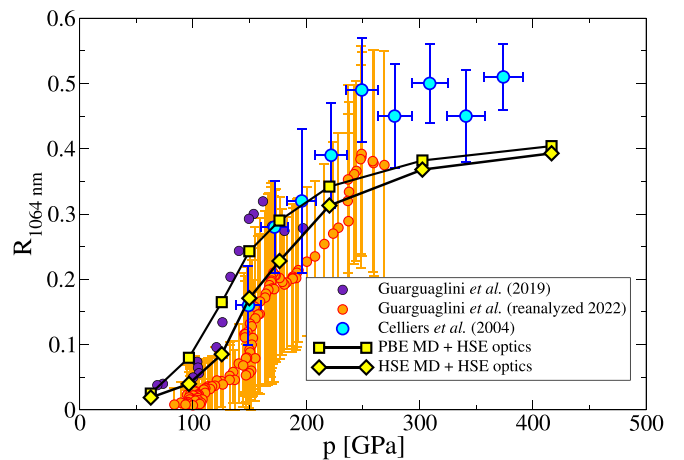


FIG. 4. 1064-nm reflectivity along the principal Hugoniot curve of water compared with the experiments of Guarguaglini *et al.* [29] and Celliers *et al.* [23]. The data from Guarguaglini *et al.* [29] were reanalyzed in this paper according to Sec. III.

on 0.1 ns interval instead of averaging over longer time intervals) and also by the use of the reference model of Brygoo *et al.* [87] at 532 nm, for which uncertainties on the different parameters were provided and are taken into account. The uncertainty of the reanalyzed reflectivity is calculated through a Monte Carlo procedure from the propagation of both experimental error bars and uncertainties of the quartz model parameters and is shown in Figs. 3, 4, 7, 8, 11, and 12. It is worth noting that these uncertainties are likely overestimated and that the shot-to-shot variability is smaller. The reanalysis of the 532 nm data gives essentially the same results as in Ref. [29] within the uncertainties, but yields very noticeable and systematic shifting of the data.

IV. RESULTS

The main results of this paper are contained in following subsections, each with a slightly different focus. Section IV A is dedicated to water at previously calculated Hugoniot states and includes a more extended discussion on the influence of the XC functional on DFT calculations of the refractive index of the unshocked state. Section IV B presents a calculated Hugoniot curve and reflectivities for a more complex mixture of water and ethanol. Results for a third component, ammonia, are given in Sec. IV C, where the discussion is completed by also examining the direct influence of the XC functional on the thermodynamic states of the Hugoniot curve.

A. Optical properties of water

At first we examine the refractive index of water at 0.998 g/cm^3 and 298 K, which corresponds to the initial conditions of the Hugoniot experiments [23,25,26,29]. We calculate n_0 with all four possible combinations of using the PBE and the HSE functional in DFT-MD and DFT optics calculations with 32 water molecules and display the results versus the photon energy, $E = \hbar\omega$, in Fig. 2.

Figure 2 shows that n_0 is primarily sensitive to the XC functional chosen in the DFT optics calculations, in which the PBE functional predicts too high values due to the underestimation of the band gap. The HSE functional offers a greatly improved description of the band gap [48] and, therefore, reproduces the experimental values [91] much better. Both PBE and HSE functional yield very similar ionic configurations in DFT-MD simulations with no thermally excited electrons [92], but a small effect on n_0 is still visible (compare solid black and blue lines in Fig. 2). From these calculations, we conclude that the consequent use of the HSE functional in our method yields the most accurate optical properties of water at ambient conditions. The interested reader will also find the electronic density of states in the Appendix. The explanation why earlier HSE calculations [42] resulted in too small values for n_0 is that contributions from the nonlocal terms of Hartree-Fock exchange term to the velocity matrix elements had not been included at that time.

Note that the oscillatory behavior in the experimental results [91] at low frequencies arises from polarization changes due to the motion of the ions, like molecular vibrations. While such contributions could be taken into account in our DFT-MD simulations, e.g., via a combination of polarization

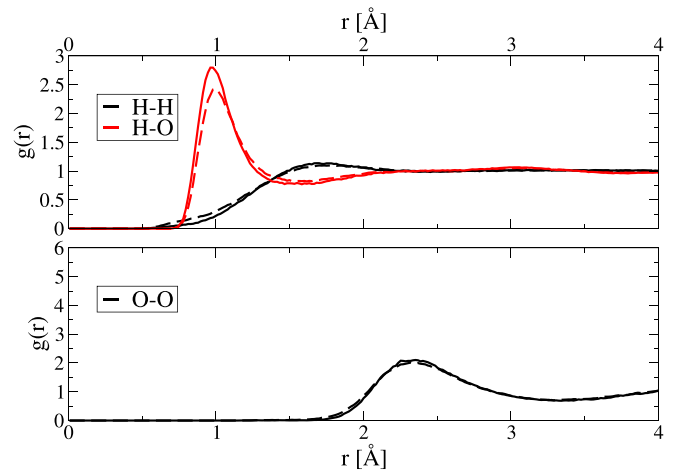


FIG. 5. Ionic pair correlation functions for water at 6000 K and 2.56 g/cm^3 , which corresponds to a Hugoniot pressure of 96.7 GPa. Solid lines are from HSE-MD simulations, while dashed lines are derived from PBE-MD simulations.

theory and Green-Kubo relation [93], we do not attempt this here. All the reflectivity measurements we compare with in this paper were made at frequencies above 1 eV, so that the contribution of ionic motions to the optical properties can be safely neglected.

We now calculate the reflectivity along the principal Hugoniot curve of water with 54 molecules up to 12 000 K and 24 molecules at higher T . Here we use previously calculated Hugoniot densities and temperatures [74] that are in good agreement with several experiments [12,25,94,95], including high-precision measurements made at the Z machine [25] as well as temperature measurements [26,29,96,97]. Knowing the poor performance of the PBE functional in predicting the index of refraction and in earlier reflectivity calculations [42], we exclusively use the HSE functional in the DFT optics calculations in the following. However, we perform these DFT calculations with two sets of ionic configurations that are generated with either the PBE or the HSE functional. The results are compared with experiments [23,25,26,29] in Figs. 3 and 4. The 532-nm results from Ref. [23] are not shown here because they are in disagreement with the other measurements and level off at far higher reflectivity values of 0.4 ± 0.1 .

The rise in reflectivity calculated from DFT-MD simulations occurs at significantly higher pressures with the HSE functional than with PBE. At pressures larger than 200 GPa, both sets of curves tend to approach each other again. This indicates that both XC functionals generate notably different ionic configurations, mostly so in the region where water becomes ionized. Using the HSE functional in both DFT-MD and DFT optics calculations results in very good agreement with the experiments at 532 nm [25,26] and reanalyzed experimental data from Ref. [29] for both 532 and 1064 nm. The very high reflectivities measured exclusively in Ref. [23] are not reproduced by any of our calculations.

To illustrate the influence of the XC functional on the ionic structure directly, we show ionic pair correlation functions for 6000 K and 2.56 g/cm^3 in Fig. 5. The ions, especially the protons, are more strongly correlated in the HSE simulations,

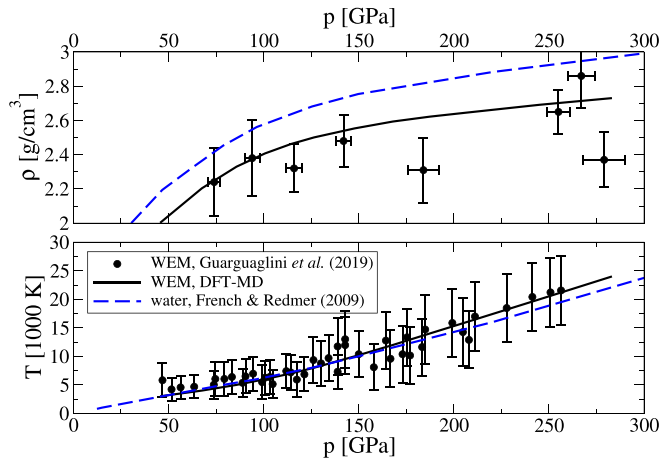


FIG. 6. Hugoniot curve of WEM calculated with DFT-MD simulations using the PBE functional in comparison with experimental data [29] and the water Hugoniot [74] used in Sec IV A.

which is an indicator for a somewhat lower degree of dissociation. Combined with our reflectivity results, this shows that dissociation and ionization are closely linked processes in compressed, partially ionized water.

B. Hugoniot curve and reflectivity of water-ethanol mixtures

The initial condition of the water-ethanol mixture (WEM) [29] is simulated with 40 water molecules and 16 ethanol molecules at 298 K and 0.8804 g/cm^3 . The DFT-MD simulation is run for 300 000 time steps, which produces sufficiently uncorrelated ionic configurations. So far, we found such a DFT-MD simulation only feasible with the PBE functional. A plot of the electronic density of states is found in the Appendix. The calculated index of refraction of this solution is $n_{0,\text{HSE}}(2.1 \text{ eV}) = 1.36$ (from HSE optics calculations) and $n_{0,\text{PBE}}(2.1 \text{ eV}) = 1.43$ (from PBE optics calculations) at optical wavelengths. The values are higher than those for pure water, see Fig. 2, but the influence of the XC functional is very similar. The experimental index of refraction for the sodium D line [98] of $n_{0,\text{exp}}(2.1 \text{ eV}) = 1.36$ agrees very well with our HSE optics calculations.

We then perform several DFT-MD simulations of WEM, all of them with the PBE functional, to calculate the Hugoniot curve with Eq. (3). At 6000 K and higher temperature, we have checked that the particle number can be reduced to 20 water molecules and 8 ethanol molecules because of strong dissociation and, thus, simplification of the occurring ionic structures. The calculated Hugoniot curve is compared with the experiments in Fig. 6. Both $p - \rho$ and $p - T$ relations are in agreement with the measurements [29]. Figure 6 also contains the Hugoniot curve for pure water [74] used in Sec. IV A for comparison, which is located at higher density but differs not much in the $p - T$ plane.

The reflectivity of the WEM is calculated by performing DFT-MD simulations with both PBE and HSE functional at four of the calculated Hugoniot densities and temperatures. Optical properties are then calculated with the HSE functional exclusively. The results are presented in Figs. 7 and 8. It is clearly seen that the simulations with the PBE functional do

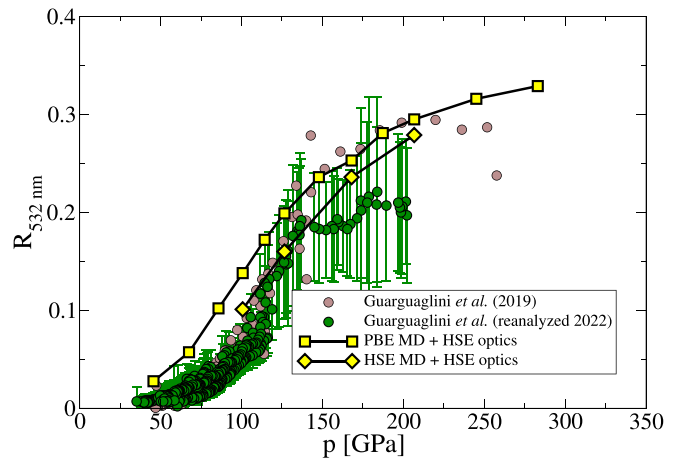


FIG. 7. 532-nm reflectivity along the principal Hugoniot curve of WEM compared with the original and reanalyzed experimental results of Guarguaglini *et al.* [29].

not accurately reproduce the rise in reflectivity, but that the full HSE calculations are close to the reanalyzed experimental data from Guarguaglini *et al.* [29]. This observation applies to both wavelengths (532 and 1064 nm).

We also examine the differences in the ionic pair correlation functions due to the XC functional at a density of 2.41 g/cm^3 and a temperature of 6000 K in Fig. 9. Similar as in Sec. IV A, the structural ionic correlations are stronger with the HSE functional than with PBE. Especially the protons tend to be more correlated with the heavy particles, which indicates a lesser degree of proton dissociation. Ionic correlations among carbon atoms are also notably enhanced, whereas the oxygen structure is only mildly affected, similar as in pure water (Fig. 5).

C. Hugoniot curve and reflectivity of ammonia

The previous sections IV A and IV B explored the influence of the XC functional on optical properties. However, the underlying Hugoniot states of water and WEM, although in

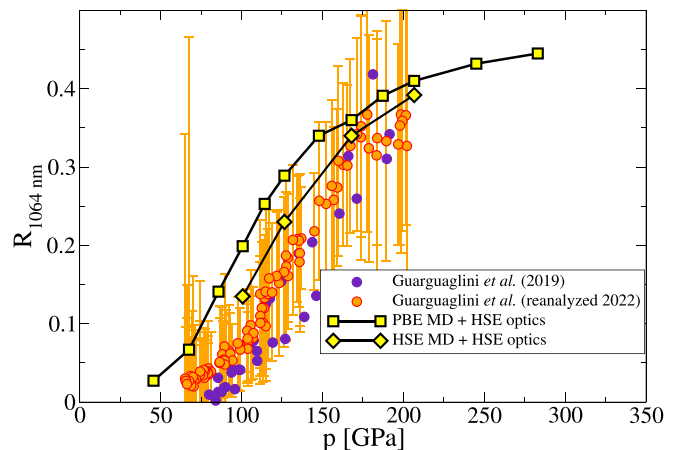


FIG. 8. 1064-nm reflectivity along the principal Hugoniot curve of WEM compared with the original and reanalyzed experimental results of Guarguaglini *et al.* [29].

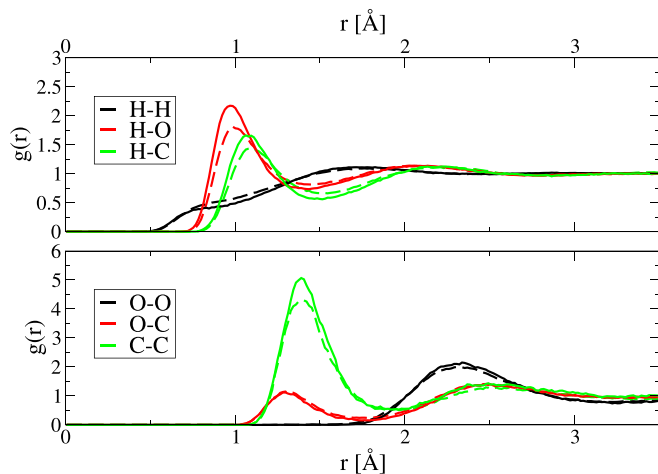


FIG. 9. Ionic pair correlation functions for WEM at 6000 K and 2.41 g/cm^3 , which corresponds to a Hugoniot pressure of 101 GPa. Solid lines are from HSE-MD simulations, while dashed lines are derived from PBE-MD simulations.

agreement with experiments, had still been derived with EOS based on DFT-MD simulations with the PBE functional. Thus, our theoretical description in Secs. IV A and IV B was not yet completely consistent in the choice of the XC functional. This section addresses this last remaining inconsistency, taking ammonia as example. We now calculate optical properties also along a Hugoniot curve that was exclusively based on a DFT-MD EOS with the HSE functional. As in a previous paper [30], all DFT-MD simulations are run with 32 ammonia molecules here.

We choose the shock wave experiment from Ravasio *et al.* [30] ($\rho_0 = 0.61 \text{ g/cm}^3$ and 295 K) as example because optical properties were measured in that experiment as well. Our calculated Hugoniot states are shown in Fig. 10. The results for the PBE calculations are the same as in Ref. [30] and are in very good agreement with the experiments. Our additional HSE calculations produce very similar states in the $p-T$ plane but show a slightly higher density compression than

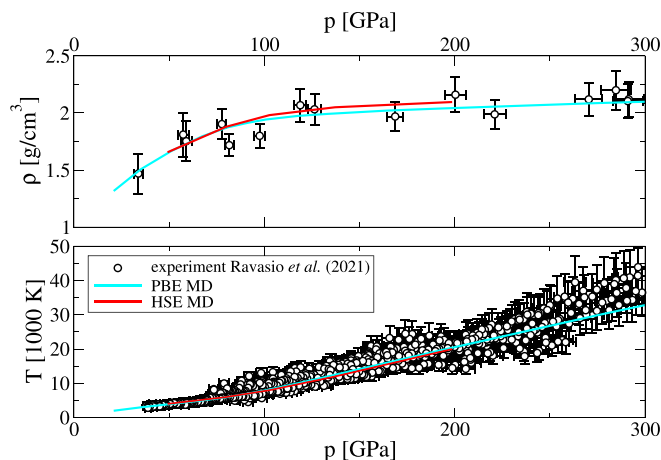


FIG. 10. Hugoniot curve of ammonia calculated with DFT-MD simulations using the PBE and HSE functionals in comparison with experimental data [30].

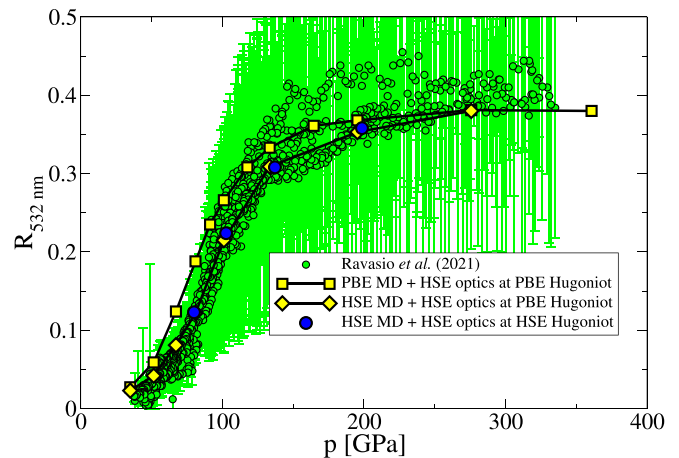


FIG. 11. 532-nm reflectivity along the Hugoniot curve of ammonia compared with the experiments of Ravasio *et al.* [30].

the PBE results. The deviation becomes notable only above 4000 K, which is where dissociation and ionization become significant. The higher density compression that occurs in the HSE calculations can be explained by smaller degrees of dissociation and ionization, which leads to fewer free particles and, consequently, a lower thermal pressure in the system.

The index of refraction for the initial Hugoniot state is calculated as $n_{0,\text{PBE-MD,HSE-optics}}(2.4 \text{ eV}) = 1.34$ and $n_{0,\text{HSE-MD,HSE-optics}}(2.4 \text{ eV}) = 1.33$. Similar as in Sec. IV A, the result from the fully consistent HSE calculation is closer to the experimental value of $n_{0,\text{exp}}(2.4 \text{ eV}) = 1.32 \pm 0.01$ [99]. The electronic densities of states for the PBE and the HSE simulations are shown in the Appendix.

The reflectivity along the Hugoniot curve is shown in Figs. 11 and 12. The DFT-MD results behave analogously to what was found in the previous sections: Using the PBE functional in the DFT-MD simulations leads to a too quick increase in the reflectivity, whereas fully consistent HSE calculations agree very well with the experimental results at 532 nm. The experimental data for 1064 nm are yet too scattered to

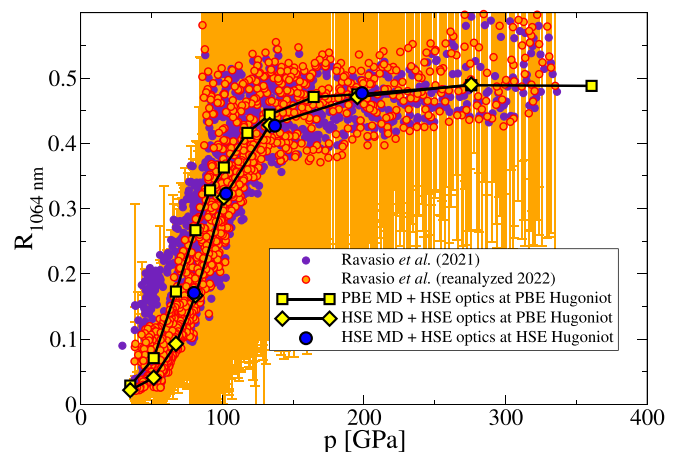


FIG. 12. 1064-nm reflectivity along the Hugoniot curve of ammonia compared with the experiments of Ravasio *et al.* [30] and their reanalyzed data.

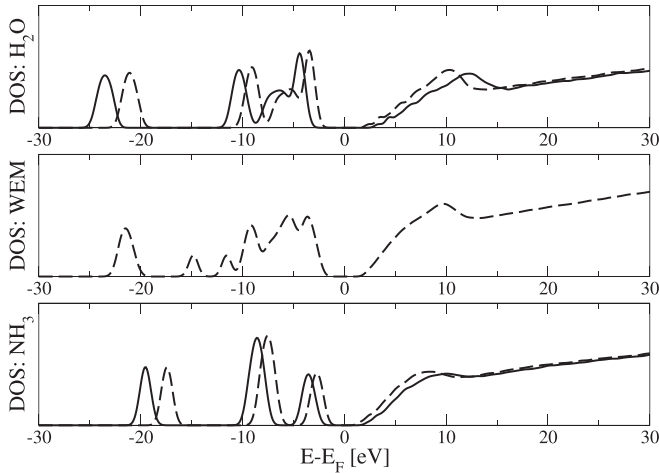


FIG. 13. Electronic density of states for water, WEM, and ammonia at their initial Hugoniot conditions. The HSE results are shown as solid lines, while the PBE results are dashed. All energies are aligned to have the Fermi energy levels E_F located at zero.

allow distinction between the theoretical curves, although the reanalysis of data improved the accuracy by narrowing the cloud of data points substantially, especially between 50 and 100 GPa.

The most important result in Figs. 11 and 12 is that the calculated reflectivity is quite insensitive to the XC functional used to determine the thermodynamic conditions of the Hugoniot (compare yellow diamonds with large blue circles). It seems sufficient to calculate the Hugoniot curve with an EOS derived with the PBE functional and then use the HSE functional consistently in the DFT-MD simulations and DFT optics calculations to determine the reflectivity. We expect this finding to be transferable to similar molecular substances like water and WEM. Therefore, we may regard the good agreement between experimental and calculated Hugoniot reflectivities found in Secs. IV A and IV B as genuine.

V. FINAL DISCUSSION AND CONCLUSIONS

In summary, we have investigated the influence of the XC functional on the optical properties of three molecular substances in shock-compressed states. Using the HSE functional, which offers an improved description of the electronic band gap, instead of the PBE functional in DFT-MD simulations leads to stronger ionic correlations that indicate a smaller degree of dissociation. This affects the EOS, but more strongly the optical properties of the substance in regions where dissociation and ionization processes occur. Our findings are supported by systematic comparisons with reflectivity measurements, which are best reproduced when the HSE functional is used consistently in both DFT-MD and DFT optics calculations.

Using an EOS derived with the PBE functional seems, nevertheless, sufficient for the calculation of thermodynamic Hugoniot states. The reason is that the current laser-driven experiments [29,30] are not accurate enough to resolve the relatively small compression differences caused by exchanging the PBE with the HSE functional. Future experiments on the

Z machine, which can achieve a much higher accuracy [25], may be required to resolve such subtle differences in density compression.

We also emphasize that determining the propagation of the probe laser through a complex experimental setup requires accurate reference standards for the optical properties of the materials involved. The respective reanalysis of the reflectivity measurements illustrates the sensitivity of the experiments to the choice of the shocked quartz reflectivity model at 1064 nm used to determine the measured reflectivity on an absolute scale. We encourage new absolute measurements of shocked quartz reflectivity at 1064 nm to resolve this uncertainty.

Further implications of our paper that are not discussed directly in this article concern the dc values of electronic conductivities [83] derived with the DFT-MD simulation technique. For molecular substances that are partially dissociated or partially ionized, these properties should preferably be determined with fully consistent HSE calculations. We can expect that previous conductivity calculations employing DFT-MD simulations with the PBE functional and computing the electronic transport properties with the HSE functional lead to somewhat overestimated numbers [30,100,101].

In addition, note that although the HSE functional seems to offer a reasonably accurate description of the electronic structure and electronic XC energies of the substances investigated here, electron-electron scattering processes are in no way included in transport properties calculated with the Kubo-Greenwood formalism as used here because DFT is an effective single-particle description of electrons [34]. Conversely, the good concordance of calculated reflectivities with the experiments suggests that electron-electron scattering does not play a significant role at the investigated densities and temperatures. This inference is plausible because the degeneracy of the electrons in the shocked materials is still relatively high, which results in strong Pauli blocking that suppresses electron-electron scattering processes [102,103].

Finally, our finding that an accurate description of the electronic band gap and electronic XC effects is necessary to properly describe dissociation and ionization transitions of molecular substances is well in line with previous DFT and quantum Monte Carlo investigations on pure hydrogen [58,104–106]. There, the location of the nonmetal-to-metal transition occurs at too low pressures when the PBE functional is used. The present calculations on water, WEM, and ammonia show the same qualitative shift, albeit these compounds dissociate and ionize continuously along their principal Hugoniot curves and no thermodynamic instabilities occur.

ACKNOWLEDGMENTS

We thank R. Redmer for helpful discussions. M.F. acknowledges support by the Deutsche Forschungsgemeinschaft (DFG) within the FOR 2440. M.B. gratefully acknowledges support by the European Horizon 2020 programme within the Marie Skłodowska-Curie actions (xICE Grant No. 894725) and the NOMIS foundation. A.R. and J.-A.H. acknowledge support from the French National Research Agency (ANR) through the projects POMPEI (Grant No. ANR-16-CE31-

0008) and SUPER-ICES (Grant No. ANR-15-CE30-008-01). The *ab initio* calculations were performed at the North-German Supercomputing Alliance (HLRN) facilities.

APPENDIX: ELECTRONIC DENSITY OF STATES

The electronic density of states for the initial Hugoniot conditions of water, WEM, and ammonia from our DFT-MD

simulations is shown in Fig. 13. In case of water and ammonia, the HSE functional results in significantly wider band gaps than PBE predicts. Because of the very high computational costs to run the DFT-MD simulations, we only have the PBE results available for WEM. The density of states was derived from the electronic energy levels using a Gaussian broadening of 0.5 eV.

- [1] R. Helled, *The Interiors of Jupiter and Saturn* (Oxford University Press, Oxford, 2019).
- [2] R. Helled, G. Mazzola, and R. Redmer, *Nat. Rev. Phys.* **2**, 562 (2020).
- [3] C. Arridge, N. Achilleos, J. Agarwal, C. Agnor, R. Ambrosi, N. André, S. Badman, K. Baines, D. Banfield, M. Barthélémy *et al.*, *Planet. Space Sci.* **104**, 122 (2014).
- [4] A. Masters, N. Achilleos, C. B. Agnor, S. Campagnola, S. Charnoz, B. Christophe, A. Coates, L. Fletcher, G. Jones, L. Lamy *et al.*, *Planet. Space Sci.* **104**, 108 (2014).
- [5] G. Schubert and K. M. Soderlund, *Phys. Earth Planet. Inter.* **187**, 92 (2011).
- [6] M. French, A. Becker, W. Lorenzen, N. Nettelmann, M. Bethkenhagen, J. Wicht, and R. Redmer, *Astrophys. J. Suppl. Ser.* **202**, 5 (2012).
- [7] J. Wicht, M. French, S. Stellmach, N. Nettelmann, T. Gastine, L. Duarte, and R. Redmer, in *Magnetic Fields in the Solar System*, Vol. 448 (Springer, Astrophysics and Space Science Library, Cham, 2018), pp. 7–82.
- [8] K. M. Soderlund and S. Stanley, *Phil. Trans. R. Soc. A.* **378**, 20190479 (2020).
- [9] Y. B. Zel'dovich and Y. P. Raizer, in *Physics of Shock Waves and High-Temperature Hydrodynamic Phenomena*, edited by W. D. Hayes and R. F. Probstein (Dover Publications Inc., Mineola, NY, 2002).
- [10] T. S. Duffy and R. F. Smith, *Front. Earth Sci.* **7**, 23 (2019).
- [11] S. D. Hamann and M. Linton, *Trans. Faraday Soc.* **62**, 2234 (1966).
- [12] A. C. Mitchell and W. J. Nellis, *J. Chem. Phys.* **76**, 6273 (1982).
- [13] S. T. Weir, A. C. Mitchell, and W. J. Nellis, *Phys. Rev. Lett.* **76**, 1860 (1996).
- [14] W. J. Nellis, N. C. Holmes, A. C. Mitchell, D. C. Hamilton, and M. Nicol, *J. Chem. Phys.* **107**, 9096 (1997).
- [15] V. V. Yakushev, V. I. Postnov, V. E. Fortov, and T. I. Yakusheva, *J. Exp. Theor. Phys.* **90**, 617 (2000).
- [16] R. Chau, A. C. Mitchell, R. W. Minich, and W. J. Nellis, *J. Chem. Phys.* **114**, 1361 (2001).
- [17] V. E. Fortov, V. Y. Ternovoi, M. V. Zhernokletov, M. A. Mochalov, A. L. Mikhailov, A. S. Filimonov, A. A. Pyalling, V. B. Mintsev, V. K. Gryaznov, and I. L. Iosilevskii, *J. Exp. Theor. Phys.* **97**, 259 (2003).
- [18] R. Chau, S. Hamel, and W. J. Nellis, *Nat. Commun.* **2**, 203 (2011).
- [19] R. S. Crum, D. A. Brantley, V. Tran, M. C. Akin, and R. Chau, *Phys. Rev. B* **104**, 184117 (2021).
- [20] V. Mintsev and Y. B. Zaporozhets, *Contrib. Plasma Phys.* **29**, 493 (1989).
- [21] G. W. Collins, P. M. Celliers, D. M. Gold, L. B. da Silva, and R. Cauble, *Contrib. Plasma Phys.* **39**, 13 (1999).
- [22] P. M. Celliers, G. W. Collins, L. B. Da Silva, D. M. Gold, R. Cauble, R. J. Wallace, M. E. Foord, and B. A. Hammel, *Phys. Rev. Lett.* **84**, 5564 (2000).
- [23] P. M. Celliers, G. W. Collins, D. G. Hicks, M. Koenig, E. Henry, A. Benuzzi-Mounaix, D. Batani, D. K. Bradley, L. B. D. Silva, R. J. Wallace *et al.*, *Phys. Plasmas* **11**, L41 (2004).
- [24] K. K. M. Lee, L. R. Benedetti, R. Jeanloz, P. M. Celliers, J. H. Eggert, D. G. Hicks, S. J. Moon, A. Mackinnon, L. B. D. Silva, D. K. Bradley *et al.*, *J. Chem. Phys.* **125**, 014701 (2006).
- [25] M. D. Knudson, M. P. Desjarlais, R. W. Lemke, T. R. Mattsson, M. French, N. Nettelmann, and R. Redmer, *Phys. Rev. Lett.* **108**, 091102 (2012).
- [26] T. Kimura, N. Ozaki, T. Sano, T. Okuchi, T. Sano, K. Shimizu, K. Miyanishi, T. Terai, T. Kakeshita, Y. Sakawa, and R. Kodama, *J. Chem. Phys.* **142**, 164504 (2015).
- [27] F. Millot, S. Hamel, J. R. Rygg, P. M. Celliers, G. W. Collins, F. Coppari, D. E. Fratanduono, R. Jeanloz, D. C. Swift, and J. H. Eggert, *Nat. Phys.* **14**, 297 (2018).
- [28] Z. He, G. Jia, F. Zhang, K. Luo, X. Huang, H. Shu, Z. Fang, J. Ye, Z. Xie, M. Xia, and S. Fu, *Eur. Phys. J. D* **72**, 3 (2018).
- [29] M. Guarguaglini, J.-A. Hernandez, T. Okuchi, P. Barroso, A. Benuzzi-Mounaix, M. Bethkenhagen, R. Bolis, E. Brambrink, M. French, Y. Fujimoto *et al.*, *Sci. Rep.* **9**, 10155 (2019).
- [30] A. Ravasio, M. Bethkenhagen, J.-A. Hernandez, A. Benuzzi-Mounaix, F. Datchi, M. French, M. Guarguaglini, F. Lefevre, S. Ninet, R. Redmer, and T. Vinci, *Phys. Rev. Lett.* **126**, 025003 (2021).
- [31] S. Brygoo, P. Loubeyre, M. Millot, J. R. Rygg, P. M. Celliers, J. H. Eggert, R. Jeanloz, and G. W. Collins, *Nature (London)* **593**, 517 (2021).
- [32] J.-A. Hernandez, M. Bethkenhagen, S. Ninet, M. French, A. Benuzzi-Mounaix, F. Datchi, M. Guarguaglini, F. Lefevre, F. Occelli, R. Redmer, T. Vinci, and A. Ravasio [Nat. Phys. (to be published)].
- [33] P. M. Celliers, P. Loubeyre, J. H. Eggert, S. Brygoo, R. S. McWilliams, D. G. Hicks, T. R. Boehly, R. Jeanloz, and G. W. Collins, *Phys. Rev. Lett.* **104**, 184503 (2010).
- [34] M. French, G. Röpke, M. Schörner, M. Bethkenhagen, M. P. Desjarlais, and R. Redmer, *Phys. Rev. E* **105**, 065204 (2022).
- [35] B. B. L. Witte, P. Sperling, M. French, V. Recoules, S. H. Glenzer, and R. Redmer, *Phys. Plasmas* **25**, 056901 (2018).
- [36] P. Hohenberg and W. Kohn, *Phys. Rev.* **136**, B864 (1964).
- [37] W. Kohn and L. J. Sham, *Phys. Rev.* **140**, A1133 (1965).
- [38] N. D. Mermin, *Phys. Rev.* **137**, A1441 (1965).
- [39] L. A. Collins, S. R. Bickham, J. D. Kress, S. Mazevet, T. J. Lenosky, N. J. Troullier, and W. Windl, *Phys. Rev. B* **63**, 184110 (2001).
- [40] S. Mazevet, M. P. Desjarlais, L. A. Collins, J. D. Kress, and N. H. Magee, *Phys. Rev. E* **71**, 016409 (2005).

- [41] B. Holst, R. Redmer, and M. P. Desjarlais, *Phys. Rev. B* **77**, 184201 (2008).
- [42] M. French and R. Redmer, *Phys. Plasmas* **18**, 043301 (2011).
- [43] L. A. Collins, J. D. Kress, and D. E. Hanson, *Phys. Rev. B* **85**, 233101 (2012).
- [44] J. Kohanoff, *Electronic Structure Calculations for Solids and Molecules* (Cambridge University Press, Cambridge, 2006).
- [45] N. Mardirossian and M. Head-Gordon, *Mol. Phys.* **115**, 2315 (2017).
- [46] P. Haas, F. Tran, and P. Blaha, *Phys. Rev. B* **79**, 085104 (2009).
- [47] F. Tran, J. Stelzl, and P. Blaha, *J. Chem. Phys.* **144**, 204120 (2016).
- [48] J. Heyd, J. E. Peralta, G. E. Scuseria, and R. L. Martin, *J. Chem. Phys.* **123**, 174101 (2005).
- [49] P. Borlido, J. Schmidt, A. W. Huran, F. Tran, M. A. L. Marques, and S. Botti, *npj Comput. Mater.* **6**, 96 (2020).
- [50] J. Heyd, G. E. Scuseria, and M. Ernzerhof, *J. Chem. Phys.* **118**, 8207 (2003).
- [51] J. Heyd, G. E. Scuseria, and M. Ernzerhof, *J. Chem. Phys.* **124**, 219906 (2006).
- [52] J. P. Perdew, K. Burke, and M. Ernzerhof, *Phys. Rev. Lett.* **77**, 3865 (1996).
- [53] S. Groth, T. Dornheim, T. Sjostrom, F. D. Malone, W. M. C. Foulkes, and M. Bonitz, *Phys. Rev. Lett.* **119**, 135001 (2017).
- [54] V. V. Karasiev, J. W. Dufty, and S. B. Trickey, *Phys. Rev. Lett.* **120**, 076401 (2018).
- [55] V. V. Karasiev, D. I. Mihaylov, and S. X. Hu, *Phys. Rev. B* **105**, L081109 (2022).
- [56] V. V. Karasiev, L. Calderín, and S. B. Trickey, *Phys. Rev. E* **93**, 063207 (2016).
- [57] V. V. Karasiev, S. X. Hu, M. Zaghoo, and T. R. Boehly, *Phys. Rev. B* **99**, 214110 (2019).
- [58] K. Ramakrishna, T. Dornheim, and J. Vorberger, *Phys. Rev. B* **101**, 195129 (2020).
- [59] S. Zhang, V. V. Karasiev, N. Shaffer, D. I. Mihaylov, K. Nichols, R. Paul, R. M. N. Goshadze, M. Ghosh, J. Hinz, R. Epstein, S. Goedecker, and S. X. Hu, *Phys. Rev. E* **106**, 045207 (2022).
- [60] Z. Moldabekov, M. Böhme, J. Vorberger, D. Blaschke, and T. Dornheim, *J. Chem. Theory Comput.* **19**, 1286 (2023).
- [61] G. Kresse and J. Hafner, *Phys. Rev. B* **47**, 558 (1993).
- [62] G. Kresse and J. Hafner, *Phys. Rev. B* **48**, 13115 (1993).
- [63] G. Kresse and J. Hafner, *Phys. Rev. B* **49**, 14251 (1994).
- [64] G. Kresse and J. Furthmüller, *Phys. Rev. B* **54**, 11169 (1996).
- [65] P. E. Blöchl, *Phys. Rev. B* **50**, 17953 (1994).
- [66] G. Kresse and D. Joubert, *Phys. Rev. B* **59**, 1758 (1999).
- [67] M. Bethkenhagen, E. R. Meyer, S. Hamel, N. Nettelmann, M. French, L. Scheibe, C. Ticknor, L. A. Collins, J. Kress, J. Fortney, and R. Redmer, *Astrophys. J.* **848**, 67 (2017).
- [68] A. Baldereschi, *Phys. Rev. B* **7**, 5212 (1973).
- [69] S. Nosé, *J. Chem. Phys.* **81**, 511 (1984).
- [70] W. G. Hoover, *Phys. Rev. A* **31**, 1695 (1985).
- [71] P. H. Berens, D. H. J. Mackay, G. M. White, and K. R. Wilson, *J. Chem. Phys.* **79**, 2375 (1983).
- [72] M. Bethkenhagen, M. French, and R. Redmer, *J. Chem. Phys.* **138**, 234504 (2013).
- [73] M. French and R. Redmer, *Phys. Rev. B* **91**, 014308 (2015).
- [74] M. French and R. Redmer, *J. Phys.: Condens. Matter* **21**, 375101 (2009).
- [75] J. W. Forbes, *Shock Wave Compression of Condensed Matter: A Primer* (Springer, Heidelberg, 2012).
- [76] R. Kubo, *J. Phys. Soc. Jpn.* **12**, 570 (1957).
- [77] D. A. Greenwood, *Proc. Phys. Soc.* **71**, 585 (1958).
- [78] Note that this procedure is only applicable to the off-diagonal matrix elements. It does not yield the correct diagonal matrix elements (electron velocities). However, those do not contribute in Eq. (4).
- [79] M. Gajdoš, K. Hummer, G. Kresse, J. Furthmüller, and F. Bechstedt, *Phys. Rev. B* **73**, 045112 (2006).
- [80] A Lorentzian function formally appears in the derivation of the Kubo-Greenwood formula, see also Eq. (6). We found no practically relevant effect on the results by using either Lorentzian or Gaussian function.
- [81] D. Zubarev, V. Morozov, and G. Röpke, *Statistical Mechanics of Nonequilibrium Processes*, Vol. I (Akademie-Verlag, Berlin, 1996).
- [82] D. Zubarev, V. Morozov, and G. Röpke, *Statistical Mechanics of Nonequilibrium Processes*, Vol. II (Akademie-Verlag, Berlin, 1997).
- [83] B. Holst, M. French, and R. Redmer, *Phys. Rev. B* **83**, 235120 (2011).
- [84] M. French, Ab-initio-Berechnung von Transporteigenschaften von warmer dichter Materie, Habilitation, Universität Rostock, 2021, https://doi.org/10.18453/rosdok_id00003719.
- [85] D. B. Melrose and R. C. McPhedran, *Electromagnetic Processes in Dispersive Media* (Cambridge University Press, Cambridge, 1991).
- [86] M. Millot, N. Dubrovinskaia, A. Černok, S. Blaha, L. Dubrovinsky, D. G. Braun, P. M. Celliers, G. W. Collins, J. H. Eggert, and R. Jeanloz, *Science* **347**, 418 (2015).
- [87] S. Brygoo, M. Millot, P. Loubeyre, A. E. Lazicki, S. Hamel, T. Qi, P. M. Celliers, F. Coppari, J. H. Eggert, D. E. Fratanduono *et al.*, *J. Appl. Phys.* **118**, 195901 (2015).
- [88] D. G. Hicks, T. R. Boehly, J. H. Eggert, J. E. Miller, P. M. Celliers, and G. W. Collins, *Phys. Rev. Lett.* **97**, 025502 (2006).
- [89] G. Huser, V. Recoules, N. Ozaki, T. Sano, Y. Sakawa, G. Salin, B. Albertazzi, K. Miyanishi, and R. Kodama, *Phys. Rev. E* **92**, 063108 (2015).
- [90] T. Qi, M. Millot, R. G. Kraus, S. Root, and S. Hamel, *Phys. Plasmas* **22**, 062706 (2015).
- [91] G. M. Hale and M. R. Querry, *Appl. Opt.* **12**, 555 (1973).
- [92] M. Guidon, F. Schiffmann, J. Hutter, and J. VandeVondele, *J. Chem. Phys.* **128**, 214104 (2008).
- [93] M. French, S. Hamel, and R. Redmer, *Phys. Rev. Lett.* **107**, 185901 (2011).
- [94] J. M. Walsh and M. H. Rice, *J. Chem. Phys.* **26**, 815 (1957).
- [95] L. P. Volkov, N. P. Voloshin, R. A. Mangasarov, V. A. Simonenko, G. V. Sin'ko, and V. L. Sorokin, *Pis'ma Zh. Eksp. Teor. Fiz.* **31**, 546 (1980) [*J. Exp. Theor. Phys. Lett.* **31**, 513 (1980)].
- [96] S. B. Kormer, *Usp. Fiz. Nauk* **94**, 641 (1968).
- [97] G. A. Lyzenga, T. J. Ahrens, W. J. Nellis, and A. C. Mitchell, *J. Chem. Phys.* **76**, 6282 (1982).

- [98] T. A. Scott, *J. Phys. Chem.* **50**, 406 (1946).
- [99] M. Gauthier, P. Pruzan, J. C. Chervin, and A. Polian, *Solid State Commun.* **68**, 149 (1988).
- [100] M. French, T. R. Mattsson, and R. Redmer, *Phys. Rev. B* **82**, 174108 (2010).
- [101] M. French and R. Redmer, *Phys. Plasmas* **24**, 092306 (2017).
- [102] R. Redmer, *Phys. Rep.* **282**, 35 (1997).
- [103] H. Reinholz, G. Röpke, S. Rosmej, and R. Redmer, *Phys. Rev. E* **91**, 043105 (2015).
- [104] W. Lorenzen, B. Holst, and R. Redmer, *Phys. Rev. B* **82**, 195107 (2010).
- [105] M. A. Morales, C. Pierleoni, E. Schwegler, and D. M. Ceperley, *Proc. Natl. Acad. Sci. USA* **107**, 12799 (2010).
- [106] C. Pierleoni, M. A. Morales, G. Rillo, M. Holzmann, and D. M. Ceperley, *Proc. Natl. Acad. Sci. USA* **113**, 4953 (2016).